JREE: Vol. 12, No. 4, (Autumn 2025) 40-52

Journal of Renewable Energy and Environment

Journal Homepage: www.jree.ir

Materials and Energy Research Center

MERC

Research Article

Design of a Switched Capacitor and Inductor-Based High Gain DC-DC Converter for DC Grid-Connected Solar PV Applications

Thamarana Sreenu, N. Shanmugasundaram*

Department of Electrical and Electronics Engineering, Vels Institute of Science, Technology and Advanced Studies, Chennai, India.

PAPER INFO

Paper history:
Received: 20 February 2025
Revised: 17 June 2025
Accepted: 22 September 2025

Keywords:
DC Microgrid,
High Gain DC-DC Converter,
MPPT,
Solar PV System

ABSTRACT

This paper proposes a novel non-isolated switched-capacitor and switched-inductor high-gain (NI-SC-SI-HG) converter for low-voltage (LV) solar photovoltaic (PV) module-fed direct-current (DC) microgrid systems. The primary objective is to achieve a high output voltage at a lower duty ratio using the NI-SC-SI-HG topology. The study investigates the voltage gain, device stresses, efficiency, and component count, with a detailed comparison to existing high-gain converters. The theoretical operation of the proposed converter is presented comprehensively, illustrating current paths under both continuous conduction mode (CCM) and discontinuous conduction mode (DCM). Mathematical analyses of each operating state are provided to support the design and performance evaluation. The proposed converter facilitates the integration of LV solar systems with DC microgrids. Additionally, its implementation in solar PV-fed applications is examined under varying irradiance conditions. Maximum power extraction is achieved using a simple perturb-and-observe (P&O) algorithm. MATLAB 2024a simulation waveforms are provided to illustrate the converter's dynamic performance. To validate the theoretical and simulation results, a 220 W, 380 V prototype of the NI-SC-SI-HG converter was developed and tested, confirming its effectiveness and practical applicability.

https://doi.org/10.30501/jree.2025.497468.2220

1. INTRODUCTION

DC-DC converters are widely used in high-voltage (HV) gain applications, including standalone systems, microgrids, and distribution networks (Arash Abedi et al., 2020). While the classic boost converter is simple and well-known, it often fails to achieve the high voltage gain required by modern applications. Conventional DC-DC boost converters face three primary limitations in high-gain scenarios (Siva Asapu et al., 2024; Nie et al., 2025; Siva Asapu et al., 2024). Due to losses in the parasitic resistances of the components, achieving high voltage gain comes at the cost of reduced efficiency.

1. High duty cycles exacerbate reverse recovery issues in the diodes.
2. The voltage stress across the switching device increases proportionally with the output voltage, resulting in higher conduction losses and the need for a high-voltage-rated switch.

These limitations make conventional boost converters unsuitable for applications requiring substantial voltage amplification. Low-voltage (LV) renewable energy systems, particularly photovoltaic (PV) systems, therefore require specialized high-gain DC-DC converters to step up the relatively low output of solar panels to levels suitable for grid integration or battery charging.

There are two types of high-gain DC-DC converters (Shokoofeh Bagheri et al., 2022): isolated and non-isolated. The potential use of non-isolated high-gain converters in microgrids, electric vehicles, and renewable energy systems has made them a hot topic in the power electronics industry (Mohammad Reza Banaei et al., 2019; Hyun Lark Do et al., 2011; Seyed Ali Akbar Fallahzadeh at al., 2021). Without the requirement for isolation transformers, non-isolated converters are more efficient, have a simpler design, and cost less than isolated converters (Hossein Gholizadeh et al., 2022). Some of the high-gain DC-DC converters are shown in Figure 1. Constant innovation is driven by the high-gain converters by the need for dependable and high-efficiency operations in this field (Rong Guo et al., 2011; Sara Hasanpour et al., 2023; M Lakshmi et al., 2018). Different topologies, design techniques, and developments in non-isolated high-gain converters were examined in this article (Sivaram Natarajan Vijayanathan et al., 2024). Including an additional subcircuit called voltage doublers (Ramachandran Rajesh et al., 2023), coupled inductors (Asapu Siva et al., 2024), switched capacitors (SC) (Mahdi Salimiet al., 2018), switched inductors (SI) (Marcos Antonio Salvador al., 2018) or combination of switched capacitor - switched inductor (SC-SI) (Keyvan Yari et al.,2024) or any energy storage-based circuit can also achieve high voltage gain. Higher voltage gains in DC-DC converters can be achieved through magnetic coupling using coupled inductors. This approach enhances efficiency and reduces input current ripple. However, it introduces design challenges, including the need for precise inductance matching and the risk of core saturation. Among the various strategies for high-gain DC-DC

*Corresponding Author's Email: *shanmugam71.se@vistas.ac.in* (Sh. N)
URL: https://www.jree.ir/article_230108.html

Please cite this article as: Thamarana, S. & N, Sh. (2025). Design of a Switched Capacitor and Inductor-based High Gain DC-DC Converter for DC Grid-Connected Solar PV Applications. *Journal of Renewable Energy and Environment (JREE)*, 12(4), 40-52. https://doi.org/10.30501/jree.2025.497468.2220.

converters, switched-capacitor and switched-inductor (SC-SI) circuits have proven to be the most effective solution.

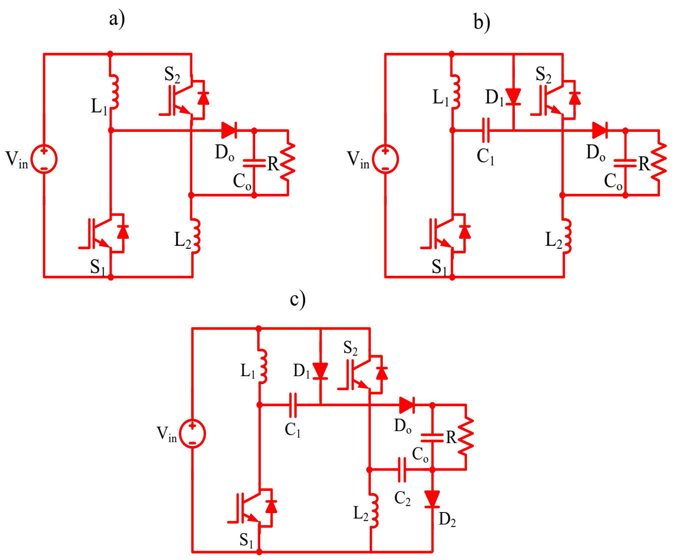

Figure 1. Circuit diagrams of high-gain converters.

Compared to existing designs, the proposed NI-SC-SI-HG converter achieves high voltage gain at a reduced duty ratio of approximately 0.6, thereby lowering the stress on switching devices. The converter features a compact structure with only one main switch, two diodes, one inductor, and two capacitors, which minimizes conduction paths and switching losses. At a test point of 54 V input and 220 W output, the proposed converter achieves an overall efficiency of 96.6% (to be confirmed through experimental or simulation validation), with a calculated total power loss of 7.48 W, including both conduction and switching losses. These results compare favorably to the 14.96 W loss and 93.2% efficiency reported for the switched-capacitor (SC) converter in Tang et al. (2015), highlighting the advantages of reduced component count and optimized operation. In addition, the voltage stress across the main switch in the proposed topology remains below 41% of the output voltage, which is significantly lower than the stress observed in conventional SC-based converters, where it often exceeds the output voltage. These improvements make the proposed converter a strong candidate for DC grid-connected solar PV systems, as it balances high voltage gain, low component count, moderate duty cycle, and competitive efficiency with reduced power loss.

A key component of today's low-voltage (LV) solar PV module-fed microgrid systems is the non-isolated high-gain converter. The block diagram of an LV-rated solar PV module-fed microgrid system with the NI-SC-SI-HG converter is presented in Figure 2. This system consists of an LV solar PV module, the NI-SC-SI-HG converter, a control system, and the microgrid interface. Continuous research in this field is driving the development of new converter topologies and designs that offer higher efficiency, improved voltage regulation, and enhanced reliability. Future studies on non-isolated high-gain converters are expected to focus on advanced control techniques, exploration of novel applications, and integration of emerging materials (Lung Sheng Yang et al., 2009; Arshad Mahmood et al., 2021; Arafa S. Mansour et al., 2022; Heidari Beni at al., 2017). Figure 1 illustrates several high-gain converters currently available, many of which achieve voltage gains comparable to, or greater than, those discussed previously. Despite this, most existing high-gain converters provide voltage gain levels that are only sufficient for integrating single-phase inverters with low-voltage (30–60 V) renewable energy sources. To address the limitations of these prior approaches, this study proposes the NI-SC-SI-HG converter, whose topology is shown in Figure 3. The main advantages of the NI-SC-SI-HG converter can be summarized as follows:

1. It achieves high efficiency and significant voltage gain without requiring an excessively high duty ratio. This enables the direct interfacing of low-voltage renewable energy sources with a 380 V microgrid.
2. The topology leverages switched capacitors and diodes to generate a larger output voltage.
3. When operating in continuous conduction mode (CCM), the converter exhibits minimal input current ripple, thereby improving the integration between the PV source and the microgrid.

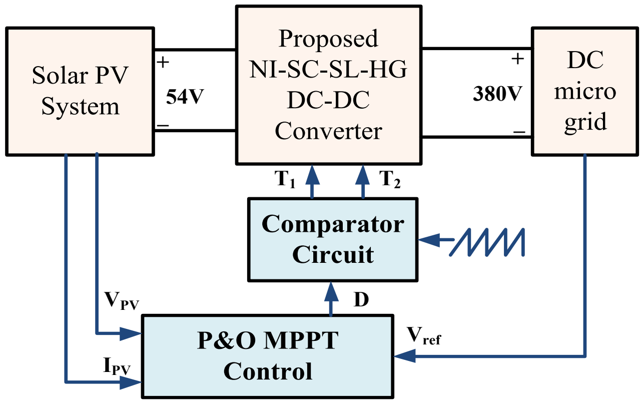

Figure 2. Microgrid system with the NI-SC-SL-HG converter and LV-rated solar PV module.

The remainder of the paper is organized as follows. Section 2 describes the operation of the NI-SC-SI-HG converter, including current circulation paths, mathematical derivation of design parameters, state-space modeling, loss analysis, and a comparative study with other high-gain converters. Section 3 discusses key design considerations of the NI-SC-SI-HG converter. Section 4 presents both simulation and hardware results: simulation results cover the NI-SC-SI-HG converter and the solar PV-fed DC grid-integrated system, while hardware validation focuses on the NI-SC-SI-HG converter. Comments and analysis related to both simulation and experimental results are also provided. Finally, Section 5 concludes the paper.

2. METHODOLOGY OF THE PROPOSED NI-SC-SL-HG CONVERTER

The proposed NI-SC-SI-HG converter for the low-voltage (LV) solar PV-fed DC microgrid system is presented in Figure 3. The converter is designed to operate in both continuous conduction mode (CCM) and discontinuous conduction mode (DCM). A resistive load R_L is connected at the output, while the corresponding waveforms for CCM and DCM operation are illustrated in Figure 4.

2.1 CCM operation

The NI-SC-SI-HG converter operates in two modes during CCM operation. Figure 5 depicts the behavior of the circuit during the first mode, and Figure 6 depicts the behavior of the circuit during the second mode.

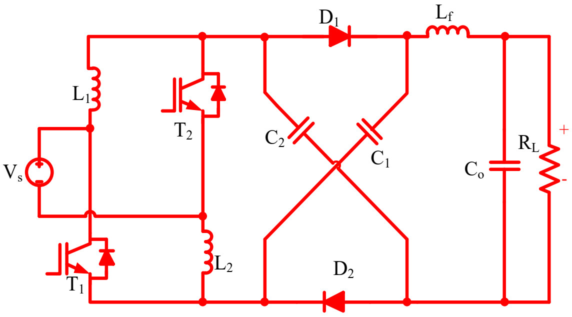

Figure 3. Circuit diagram of the NI-SC-SI-HG converter.

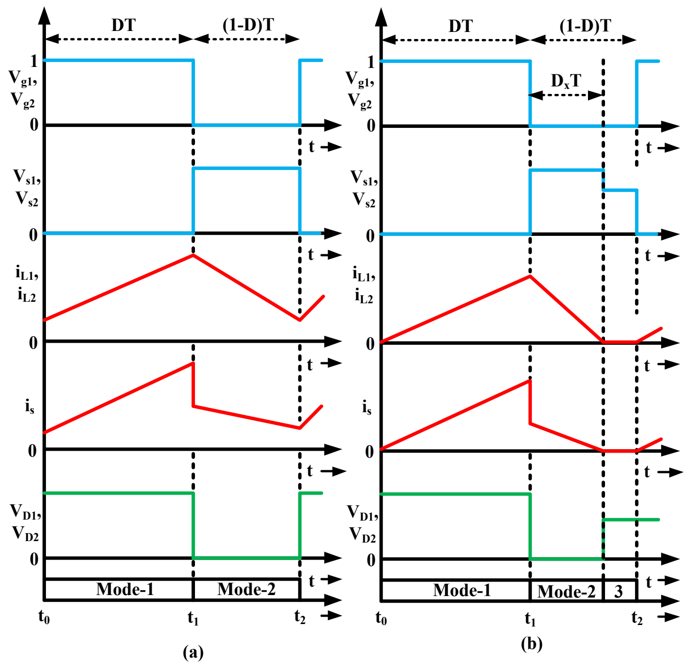

Figure 4. The NI-SC-SI-HG converter operational waveforms under (a) CCM and (b) DCM.

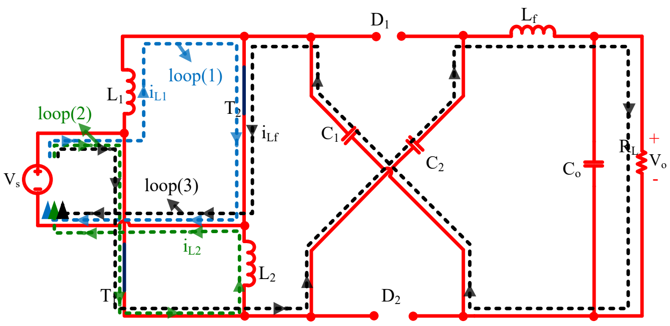

Figure 5. Equivalent circuit of the NI-SC-SI-HG converter when switches T_1 and T_2 are ON

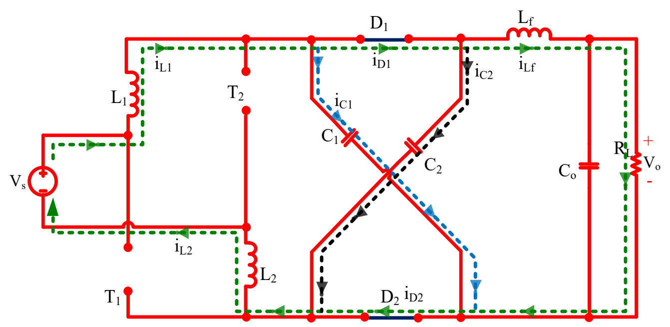

Figure 6. Equivalent circuit of the NI-SC-SI-HG converter when switches T_1 and T_2 are OFF

The first mode ($t_0 < t < t_1$): In this mode, the switches of the NI-SC-SI-HG converter T_1 and T_2 are turned ON. When both switches are turned ON, the inductors L_1 and L_2 are connected in parallel, and this parallel combination of inductors is connected to voltage source V_S. Thus, these inductors are charged linearly from V_S. By applying KVL to loop 1 and loop 2 in Figure 5, the inductor's voltages V_{L1} and V_{L2} are expressed as

$$V_S = V_{L1} = V_{L2} \tag{1}$$

$$V_{L1} = L_1 \frac{di_{L1}}{dt} \& V_{L2} = L_2 \frac{di_{L2}}{dt} \tag{2}$$

From the above equations, L_1 and L_2 are charged linearly, and the voltage across the inductors is constant which becomes input voltage V_S.

The voltage across the filter inductor can be expressed as follows:

$$V_{Lf} = 2V_C + V_S - V_O \tag{3}$$

In this mode of operation, the diodes D_1 and D_2 of the NI-SC-SI-HG converter are reverse-biased, and their currents i_{D1} and i_{D2} are zero. The reverse blocking voltages across the diodes V_{D1} and V_{D2} are equal to the peak output voltage, $V_{O(peak)}$. Under these conditions, the load is directly connected to the voltage source and the capacitors in the circuit. Capacitors C_1 and C_2 are connected in series, discharging their stored energy through the load resistor R_L. Accordingly, the output voltage v_o can be expressed in terms of the capacitor voltages as:

$$v_O = V_S + v_{C1} + v_{C2} \tag{4}$$

If C_1=C_2=C and under a steady-state condition as well as if V_{C1}=V_{C2}=V_C, the above equations become

$$v_O = V_S + 2v_C \tag{5}$$

$$V_S = V_{L1} = V_{L2} \tag{6}$$

In this mode, the source carries the inductor's charging currents (i_{L1} and i_{L2}) and the capacitor's discharging currents (i_{C1} or i_{C2}). The current paths of inductors and capacitors are shown in Figure 5. The source current i_S can be expressed as follows:

$$i_S = i_{L1} + i_{L2} + i_C \tag{7}$$

The second mode ($t_1 < t < t_2$): In this mode, T_1 and T_2 are turned OFF. When both switches are turned OFF, the L_1 and L_2 are connected in series, and this series combination of inductors discharges the stored energy to the load and capacitors. By applying KVL to loop 1 in Figure 6, the inductor's voltages V_{L1} and V_{L2} are expressed as follows:

$$-V_S - V_{L1} + V_{C1} - V_{L2} = 0 \tag{8}$$

where V_{L1}=V_{L2}=V_L and V_{C1}=V_{C2}=V_S.

$$V_{L1} = V_{L2} = \frac{V_S - V_{C1}}{2} = \frac{V_S - V_C}{2} \tag{9}$$

$$V_{L1} = V_{L2} = \frac{V_S - V_{C2}}{2} = \frac{V_S - V_C}{2} \tag{10}$$

From the above equations, L_1 and L_2 are discharged and the voltage across the inductors becomes an input voltage. The D_1 and D_2 operate in a forward biasing mode and the diode currents i_{D1} and i_{D2} are expressed as follows:

$$i_{D1} = i_{L1} - i_{C1} \tag{11}$$

$$i_{D2} = i_{L2} - i_{C2} \tag{12}$$

In this mode, C_1 and C_2 are connected in parallel, and this parallel combination of capacitors is connected to a series combination of inductors (L_1, L_2) and voltage source VS. C_1 and C_2 absorb energy from both the input source and the inductor. Under this condition, the output voltage V_O can be expressed in terms of input voltages and inductor voltages. Applying the volt–second balance principle to the inductor, and using the relations derived in equations (1) and (9), we have:

$$V_S D + \left(\frac{V_S - V_C}{2}\right)(1 - D) = 0 \tag{13}$$

Capacitor voltages can be expressed as follows:

$$V_{C1} = V_{C2} = V_C = \frac{V_O - V_S D}{1 + D} \tag{14}$$

In CCM, the converter voltage gains A_{CCM} obtained by solving the above equations (13) and (14)

$$A_{CCM} = \frac{V_O}{V_S} = \frac{1+3D}{1-D} \tag{15}$$

2.2 DCM operation

Due to the lower inductance value, the inductor current falls to zero more quickly, which results in maximum inductor charging and consequently an increase in the output voltage V_O. However, as the output voltage gain increases, the overall performance of the NI-SC-SI-HG converter tends to degrade. Therefore, the inductor must be carefully selected to achieve the desired balance between voltage gain and system performance. In the discontinuous conduction mode (DCM), the converter operates in three distinct modes. The first and second modes closely resemble those of continuous conduction mode (CCM). After the completion of these two stages, the third mode of operation begins, as illustrated in Figure 7.

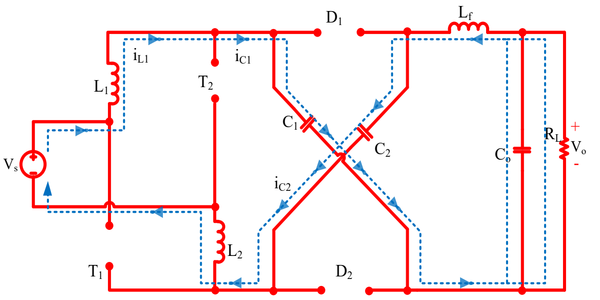

Figure 7. Equivalent circuit of NI-SC-SI-HG converter under DCM Operation.

Boundary conditions in converters are critical for analyzing their operation, particularly when transitioning between continuous conduction mode (CCM) and discontinuous conduction mode (DCM). These conditions directly affect many control strategies, such as voltage-mode and current-mode control, since the control loop compensation and dynamic response can vary depending on the operating mode. Therefore, understanding and accounting for boundary conditions is essential for accurate design and stable performance. The boundary condition is defined as the load or current level at which the converter transitions between CCM and DCM. For the proposed NI-SC-SI-HG converter, this boundary state is illustrated in Figure 8. Furthermore, the average output current under CCM (A_{CCM}) as a function of duty ratio is presented in Figure 9. This graph provides insights into the converter's performance in CCM, highlighting how practical converters diverge from their ideal theoretical characteristics as the duty cycle increases. The difference between the experimental and theoretical curves reflects efficiency variations and practical limitations such as parasitic losses and non-ideal device behavior. From Figure 9, it can be observed that the deviation between experimental and theoretical results is minimal, indicating that the proposed NI-SC-SI-HG converter closely follows the predicted performance under CCM operation.

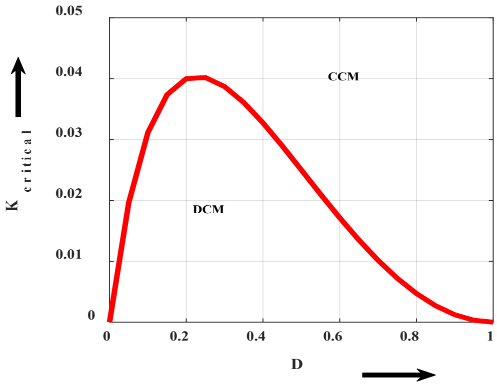

Figure 8. Boundary state of NI-SC-SI-HG converter

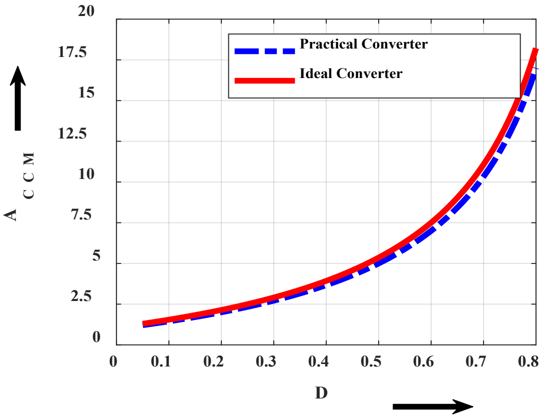

Figure 9. The voltage gain (A_{CCM}) and Duty ratio (D).

2.3 Design of proposed converter

The V_C can be expressed as follows:

$$V_C = \frac{V_S + V_O}{2} \tag{16}$$

By substituting Equation (16) in (3), the voltage across the filter inductor can be expressed as

$$V_{L_f} = L_f \frac{di_{Lf}}{dt} = 2V_S \tag{17}$$

The filter inductor can be expressed as

$$L_f = \frac{2V_S D}{f_{sw} \Delta I_{Lf}} \tag{18}$$

To obtain the expression for the design of L_1 and L_2, a similar procedure can be applied:

$$L = L_1 = L_2 = \frac{V_S D}{f_{sw} \Delta I_L} \tag{19}$$

During the time interval, the filter inductor current is the same as capacitor current i_{C1} or capacitor current i_{C2}. Therefore, we have:

$$C = C_1 = C_2 = \frac{V_O I_O D}{V_S f_{sw} \Delta V_C} \frac{(1-D)}{(1+3D)} \tag{20}$$

Capacitor voltage and inductor currents can be written as a function of the source of the converter as expressed below:

$$V_C = V_{C1} = V_{C2} = V_S \frac{(1+D)}{(1-D)} \tag{21}$$

$$I_L = I_{L1} = I_{L2} = \frac{V_O I_O}{V_S}\frac{(1-D)}{(1+3D)} \quad (22)$$

The converter circuit parameters are calculated using Eqs. (18), (19), and (20) and the values displayed in Table 2. To calculate the L1 and L_2 values, the inductor current ripple Δi_L is assumed as 20% and to calculate the capacitor values, the capacitor voltage ripple is assumed as 5%. The switching frequency 'f_s' of the converter is 50kHz.

2.4 State-space modeling and small-signal analysis

The NI-SC-SI-HG converter is modeled using the state-space averaging method to analyze its dynamic behavior. The chosen state variables are the inductor currents i_{L1}, i_{L2} and the capacitor voltages v_{C1}, v_{C2} and v_{C0}. The converter parameters used in this analysis are as follows: input voltage Vs = 54 V, Vo = 380 V, load power Po = 220 W, load resistance R_L = 220 Ω, $L_1 = L_2$ = 220 µH, L_f = 2.2 mH, $C_1 = C_2 = C_0$ = 1 µF. The operating duty cycle is chosen as D, which provides the required high voltage gain. During the switch ON state, the converter dynamics are represented by the state-space matrices A_1 and B_1, given in Equations (23) and (24). During the switch OFF state, the converter dynamics are represented by the state-space matrices A_2 and B_2, given in Equations (25) and (26).

$$A_1 = \begin{bmatrix} 00000 \\ 00000 \\ 00000 \\ 00000 \\ 0000-\frac{1}{R_L C_0} \end{bmatrix} \quad (23)$$

$$B_1 = \begin{bmatrix} \frac{1}{L_1} \\ \frac{1}{L_2} \\ 0 \\ 0 \\ 0 \end{bmatrix} \quad (24)$$

$$A_2 = \begin{bmatrix} 00-\frac{1}{L_1}00 \\ 000-\frac{1}{L_2}0 \\ \frac{1}{C_1}000-\frac{1}{C_1 L_f} \\ 0\frac{1}{C_2}00-\frac{1}{C_2 L_f} \\ 00\frac{1}{C_o L_f}\frac{1}{C_o L_f}-\frac{1}{R_L C_0}-\frac{1}{C_o L_f} \end{bmatrix} \quad (25)$$

$$B_2 = \begin{bmatrix} \frac{1}{L_1} \\ \frac{1}{L_2} \\ 0 \\ 0 \\ 0 \end{bmatrix} \quad (26)$$

The small-signal transfer function $G(s) = \frac{\hat{v}_{c0}(s)}{\hat{d}(s)}$ was derived from the averaged state-space model using the perturbation duty matrix

$$\begin{cases} \dot{x} = A\hat{x} + B\hat{d} \\ \dot{y} = C\hat{x} \end{cases} \quad (27)$$

where A and B are matrices, expressed in Equations (28) and (29):

$$A = DA_1 + (1-D)A_2 \quad (28)$$

$$B = (A_1 - A_2)X + (B_1 - B_2)V_S \quad (29)$$

The typical form of the PID controller equation expressed in Equation (30):

$$PID(s) = K_p + \frac{K_i}{s} + K_d s \quad (30)$$

A PID controller was designed to regulate the output voltage (V_O) of the proposed NI-SC-SI-HG converter. The linearized state-space model of the converter was used to derive the control-to-output transfer function, which served as the basis for controller design. MATLAB's *pidtune* tool was employed, with Ziegler–Nichols tuning rules used as an initial baseline. After refinement, the PID controller gains were selected as Kp = 1.8, Ki = 250, and Kd = 0.0009. These values were chosen to satisfy both settling time and overshoot performance criteria. The designed controller was validated through time-domain simulations under step-load variations and irradiance change conditions, confirming its effectiveness in maintaining a stable and regulated output voltage.

2.5. Efficiency and losses analysis

The power loss analysis of the NI-SC-SI-HG converter was performed using its equivalent circuit, as illustrated in Figure 10. This circuit allows for the evaluation of the converter's non-ideal characteristics by accounting for factors such as the equivalent series resistance (ESR) of the inductors and capacitors, the conduction and switching losses of the semiconductor switches, and the forward voltage drop across the diodes. The total losses of the switch can be expressed by Equation (31):

$$P_{S(total)} = P_{S(cond)} + P_{S(switch)} \quad (31)$$

When both T_1 and T_2 are turned ON, the system experiences switching and conduction losses, which can be described by the following expressions (32) and (33):

$$P_{S(switch)} = \frac{P_{T1}T_{(ON+OFF)}f_S}{2} + \frac{P_{T2}T_{(ON+OFF)}f_S}{2} \quad (32)$$

$$P_{S(cond)} = [I^2_{T1(rms)}r_{T1} + I^2_{T2(rms)}r_{T2}] \quad (33)$$

where 'r_{T1}' and 'r_{T2}'are the ON time resistances of the T_1 and T_2, respectively. The D_1 and D_2 total power loss can be expressed in expressions (34), (35), and (36):

$$P_{D(r_D)} = [I^2_{D1(rms)}r_{D1} + I^2_{D2(rms)}r_{D2}] \quad (34)$$

$$P_{D(V_F)} = [I_{D1(avg)}V_{F1} + I_{D2(avg)}V_{F2}] \quad (35)$$

$$P_{D(total)} = P_{D(r_D)} + P_{D(V_F)} \quad (36)$$

where 'r_{D1}' and 'r_{D2}'are the ON time resistances of D_1 and D_2, respectively. V_{F1} and V_{F2} are the forward voltage drop of the didoes D_1 and D_2, respectively. Similarly, the power loss of the passive components is expressed in Equations (37) and (38):

$$P_{L(total)} = [I^2_{L1(rms)}r_{L1} + I^2_{L2(rms)}r_{L2} + I^2_{Lf(rms)}r_{Lf}] \quad (37)$$

$$P_{C(total)} = [I^2_{C1(rms)}r_{C1} + I^2_{C2(rms)}r_{C2} + I^2_{Co(rms)}r_{Co}] \quad (38)$$

where r_{L1}, r_{L2}, and r_{Lf} are the ESR resistances of the L_1, L_2, and L_f, respectively. r_{C1}, r_{C2}, and r_{Co} are the ESR resistances of L_1, L_2, and L_f, respectively. From the above equations, the total power loss and efficiency of the converter are expressed in Equations (31) and (32):

$$P_{(Total-Loss)} = P_{S(total)} + P_{D(total)} + P_{L(total)} + P_{C(total)} \quad (39)$$

$$\eta = \frac{P_o}{P_o - P_{(Total-Loss)}} \times 100 \quad (40)$$

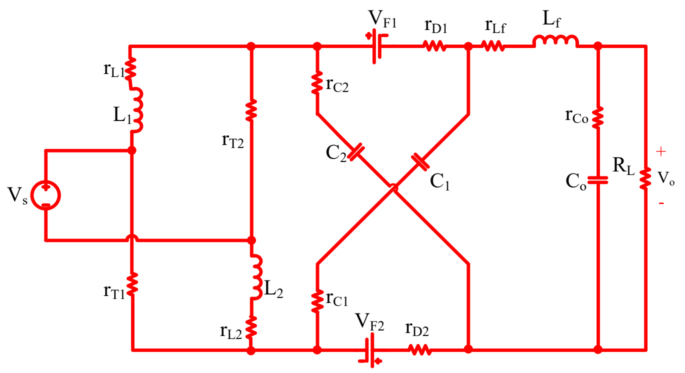

Figure 10. Equivalent circuit of the NI-SC-SI-HG converter for non-ideal conditions.

A detailed loss analysis of the proposed NI-SC-SI-HG converter was carried out to validate its efficiency under full-load conditions. The primary loss components considered include the conduction and switching losses of the MOSFETs, the conduction losses of the diodes, copper losses in the inductors, and ESR losses in the capacitors.

The MOSFET conduction losses were estimated at approximately 1.72 W, while the switching losses contributed about 3.42 W. The diode conduction losses accounted for around 0.84 W of the total loss. The combined copper losses in L1, L2, and Lf were calculated to be about 1.31 W, and the ESR losses in the capacitors were approximately 0.19 W. Summing these components, the total power loss at the rated output was found to be 3.74 W, resulting in an overall efficiency of approximately 96.6 %.

2.6. Comparative analysis

For real-time applications, it is crucial to consider the number of devices and components during the design process. Multiple studies have focused on reducing the number of devices to maximize efficiency. In a converter, conduction and switching losses are the primary contributors to total losses. In this section, the performance of the proposed converter is compared with that of previously reported converters to validate the proposed configuration.

Table 1 presents the results of a comprehensive comparative study, which analyzed the number of switches, diodes, inductors, and capacitors used in each design.

For a DC-DC converter to operate effectively with the load or downstream components, the voltage gain must be sufficiently high to regulate the input voltage (VS) to the desired output. When dealing with variable input voltages, such as those from renewable energy sources (solar or wind), a converter with a high and efficient voltage gain ensures a stable output, enabling optimal performance and maximum energy transfer. Additionally, systems requiring maximum power point tracking (MPPT) benefit significantly from converters with an appropriate voltage gain, as this enhances overall efficiency, reduces power losses, and allows the converter to handle a wide range of input conditions effectively.

The relationship between voltage gain and duty ratio, along with comparisons among different converters, is shown in Figure 11 and 12. This figure demonstrates that the NI-SC-SI-HG converter achieves a very high voltage gain when the duty ratio exceeds 0.4.

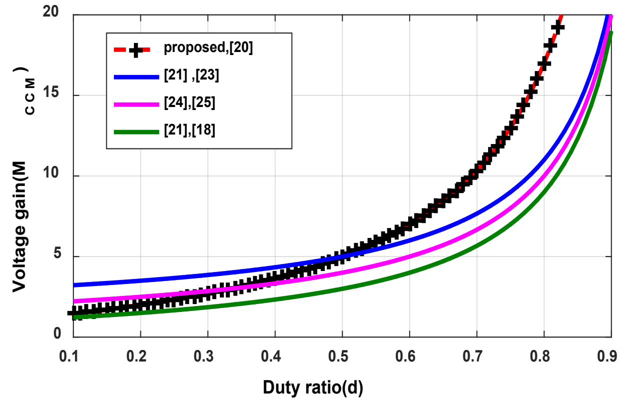

Figure 11. Comparative performance analysis - Gain plot

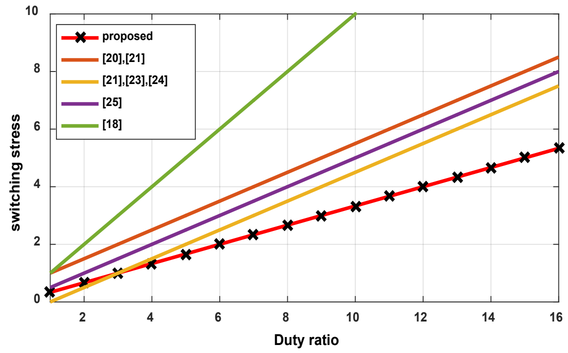

Figure 12. Comparative performance analysis - Switching stress

3. DESIGN CONSIDERATIONS

The design of passive components, such as inductors and capacitors, in the NI-SC-SI-HG converter is critical for ensuring reliable operation and achieving high voltage gain. Small variations in inductor parameters or imperfections in magnetic coupling can lead to voltage peaks across the switches. While combining inductors on a shared core improves power density, it does not completely eliminate these effects. In the proposed topology, the two input inductors have identical inductance values and operate under the same conditions, resulting in equal average voltages across the capacitors C1 and C2 (VC = VC1 = VC2 = VS + Vo/2).

Although the capacitors maintain balanced average voltages, mismatches can still cause current spikes; however, the presence of inductors helps limit these spikes. Using capacitors with tight tolerances further reduces the risk of significant peak currents through the diodes. For the active switches, two main challenges arise. First, possible resonant effects involving the input voltage, inductors, and parasitic capacitances can occur when the switches turn off. Second, voltage stresses can result from timing mismatches in the control signals. Both phenomena can increase voltage stress on the switches. Fortunately, clamping circuits can be implemented to protect the switches and enhance converter reliability. Overall, careful component selection and thoughtful design strategies help mitigate these non-ideal behaviors, improving the performance and robustness of the converter.

3.1. Inductor design

The inductance value is determined using the mathematical expression given in equation (19). Since the operating conditions of the two input inductors in the proposed topology are identical, the inductance values L1 and L2 are equal.

Table 1. Study of comparison.

S. No.	Converters	C	L	Diodes	Switches	Device voltage stress (Switches)	Device voltage stress (Diode)	Gain (A_{CCM})	Device Current Stress (Switch)	Device Current Stress (Diode)	Efficiency
1	Proposed	3	3	2	2	$\frac{A_{ccm}}{(1+3D)}$	$\frac{2A_{ccm}}{(1+3D)}$	$\frac{(1+3D)}{(1-D)}$	$\frac{D}{(1-D)}$	$\frac{1}{(1-D)}$	96.6% at 220W
2	[12]	4	1	4	1	$\frac{(A_{ccm}-1)}{2}$	-	$\frac{(3-D)}{(1-D)}$	$\frac{1}{(1-D)}$	$\frac{1}{(1-D)}$	96.8% at 220W
3	[13]	3	2	3	2	$\frac{(A_{ccm}+1)}{2}$	$(A_{ccm}-1)$	$\frac{(1+2D)}{(1-D)}$	$\frac{0.5}{D(1-D)}$	$\frac{1-D+D^2}{(1-D)}$	95.6% at 220W
4	[14]	1	2	1	1	A_{ccm}	A_{ccm}	$\frac{(1+D)}{(1-D)}$	$\frac{D}{(1-D)}$	$\frac{1}{(1-D)}$	93.8% at 200W
5	[15]	3	1	3	1	$\frac{A_{ccm}}{2}$	$\frac{A_{ccm}}{2}$	$\frac{2}{(1-D)}$	$\frac{D}{(1-D)}$	$\frac{1}{(1-D)}$	92.8% at 150W
6	[16]	1	4	7	2	$\frac{(M_{ccm}+1)}{2}$	$(A_{ccm}+1)$	$\frac{(1+3D)}{(1-D)}$	$\frac{2}{(1-D)}$	$\frac{2D}{(1-D)}$	95.1% at 220W
7	[17]	2	3	6	1	$\frac{2DA_{ccm}}{(D(3-D))}$	-	$\frac{D(3-D)}{(1-D)}$	$\frac{(1+D)}{(1-D)}$	$\frac{(1+D)}{(1-D)^2}$	95.6% at 200W
8	[18]	2	2	3	1	$\frac{A_{ccm}}{(D(2-D))}$	-	$\frac{D(2-D}{(1-D)}$	$\frac{0.5}{D(1-D)}$	$\frac{1-D+D^2}{(1-D)^2}$	94.7% at 200W
9	[19]	1	2	1	2	A_{ccm}	A_{ccm}	$\frac{(1+2D)}{(1-D)}$	$\frac{D}{(1-D)}$	$\frac{1}{(1-D)}$	93.6% at 320W
10	[21]	3	2	3	1	$\frac{A_{ccm}}{2.5}$	$\frac{A_{ccm}}{2}$	$\frac{2}{(1-2D)}$	$\frac{(1+D)}{(1-D)}$	$\frac{D(1+D)}{(1-D)^2}$	93.4% at 200W
11	[23]	1	4	6	2	$\frac{(A_{ccm}+2)}{2}$	$(A_{ccm}+1)$	$\frac{(1+2D)}{(1-D)}$	$\frac{(1+D)}{(1-D)}$	$\frac{D(1+D)}{(1-D)}$	97.2% at 50W
12	[24]	1	2	2	1	$\frac{A_{ccm}}{2.5}$	-	$\frac{D(3-D)}{(1-D)}$	$\frac{(1+D)}{(1-D)}$	$\frac{(1+D)}{(1-D)^2}$	92.3% at 100W

The switching frequency (fSW), input voltage (Vs), duty ratio (D), and inductor current ripple (ΔIL) are 50 kHz, 54 V, 0.6, and 3 A, respectively, as expressed in equation (41).

$$L = L_1 = L_2 = \frac{V_S D}{f_{sw}\Delta I_L} = \frac{54\times0.6}{50k\times3} \approx 220\mu H \quad (41)$$

3.2. Capacitor design

The capacitance value is determined using the mathematical expression given in equation (20). Since the operating conditions of the two capacitors in the proposed topology are identical, the capacitance values C1 and C2 are equal. The switching frequency (fSW), input voltage (VS), duty ratio (D), output voltage (V0), output current (I0), and capacitor voltage ripple (ΔVc) are 50 kHz, 54 V, 0.6, 380 V, 0.58 A, and 7 V, respectively, as expressed in equation (42).

$$\begin{cases} C = C_1 = C_2 = \frac{V_O I_O D}{V_S f_{sw} \Delta V_C}\frac{(1-D)}{(1+3D)} \\ C = C_1 = C_2 = \frac{380\times0.58\times0.6}{54\times50k\times7} \times \frac{(1-0.6)}{(1+(3\times0.6))} \approx 1\mu F \end{cases} \quad (42)$$

4. RESULTS AND DISCUSSION

To evaluate the performance of the NI-SC-SI-HG converter, it was successfully implemented in MATLAB simulation software. The results under CCM operation are presented in Figure 13-19. An input voltage of 54 V was applied to the converter, and to achieve an output voltage (VO) of 380 V, the converter was operated with a duty ratio of 0.6 and a switching frequency of 50 kHz.

4.1. Simulation results

As shown in Figure 13, for a duty ratio of 0.6, the converter delivers an output power of 220 W, with a variation of approximately 1% in the output voltage. At this duty ratio, the output voltage ranges between 377 V and 380 V. The waveforms of both VO and PO under steady-state conditions are presented in Figure 14. Figure 14 also illustrates the converter's transient behavior. When excited by a VS of 54 V, the maximum voltage at the load terminal reaches 673 V during transient conduction at 37.6 ms, and the transients decay within 4 ms.

For a brief period of 37.6 ms, the load withstands a voltage up to 680 V. The transient decay time depends on the duty ratio and converter parameters. The output voltage and power stabilize in approximately 0.004 s, indicating the converter’s response time. The observed overshoot in voltage and power reflects an underdamped system, which may be acceptable depending on the application. Once stabilized, the converter maintains a consistent voltage and power output, demonstrating reliable performance after transients.

The step response analysis of the converter is shown in Figures 15 and 16. The step input voltage waveform in Figure 15(a) represents a sudden increase in VS applied to the converter. Initially, the voltage is zero, indicating no input. At around 20 µs, the voltage abruptly rises from 0 V to 54 V with a rise time of 1.25 µs and remains constant, forming a typical step input. This type of input is commonly used in simulations to study the dynamic and transient response of power electronic converters or control systems under sudden changes.

In response to the step input shown in Figure 15(a), Figure 15(c) shows the VO of the converter. As VS suddenly rises to 54 V at 20 µs with a rise time of 2.5 µs, the output voltage exhibits a sharp initial increase, peaking at approximately 650 V. This peak represents the transient overshoot typical of high-gain DC-DC converters under sudden input changes. After reaching its maximum, V_O gradually settles toward a steady-state value near 380 V at a duty ratio of 0.6, with minor oscillations due to system dynamics and switching effects. Figure 15(d) depicts the corresponding output power PO. The power rises sharply during the voltage build-up, reaching a transient peak of nearly 800 W, then decreases and stabilizes, following the output voltage behavior as the converter attains steady-state operation. Similarly, the step input waveform in Figure 16(a) represents a sudden increase in VS. Initially, VS is 36 V. At around 3.5 ms, the voltage abruptly rises from 36 V to 54 V with a rise time of 0.4 µs and remains constant, forming a standard step input. Figure 16(c) shows the corresponding V_O of the converter. Following the step input, V_O initially rises sharply, reaching a peak of nearly 480 V, reflecting the transient overshoot typical of converter systems during sudden input changes. Subsequently, V_O gradually settles toward a steady-state value of approximately 380 V at a duty ratio of 0.6, with oscillations caused by the system's dynamic response and switching action. Figure 16(d) illustrates the corresponding output power PO. The power exhibits a transient peak of nearly 450 W before gradually stabilizing around 220 W, mirroring the output voltage profile. These responses demonstrate the converter's transient behavior and its capability to regulate output during step changes in input voltage.

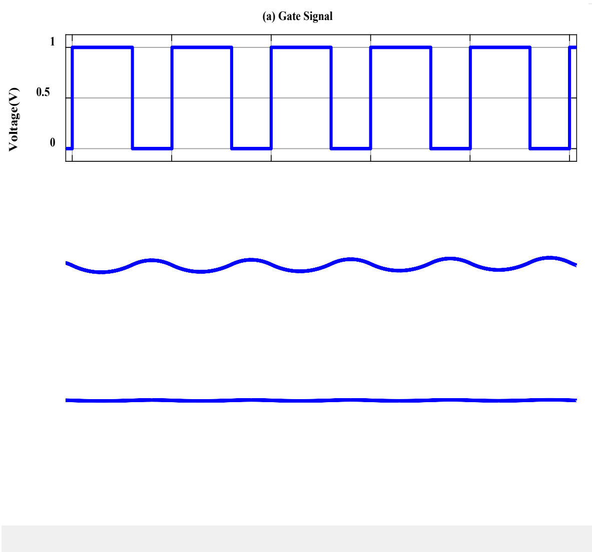

Figure 13. Output power and voltage of the NI-SC-SI-HG converter (Zoomed version of Figure 14.)

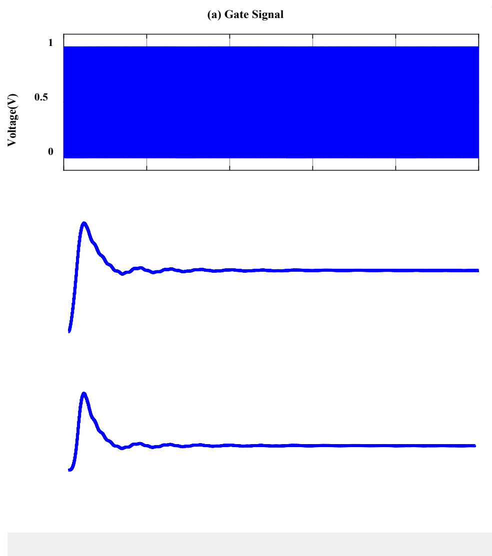

Figure 14. Output power and voltage of the NI-SC-SI-HG converter

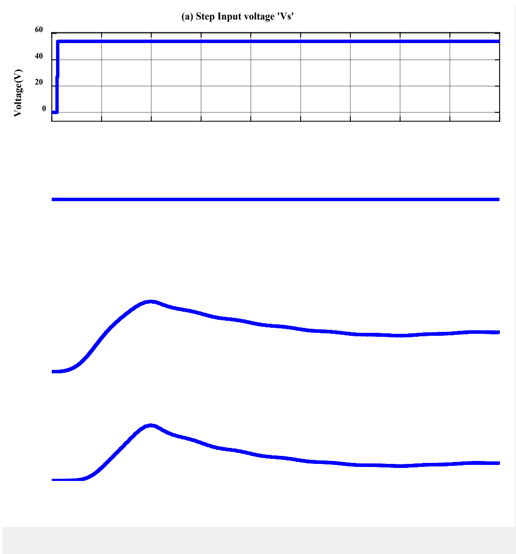

Figure 15. Dynamic performance of the NI-SC-SI-HG converter for a step input rise from 0V to 54V.

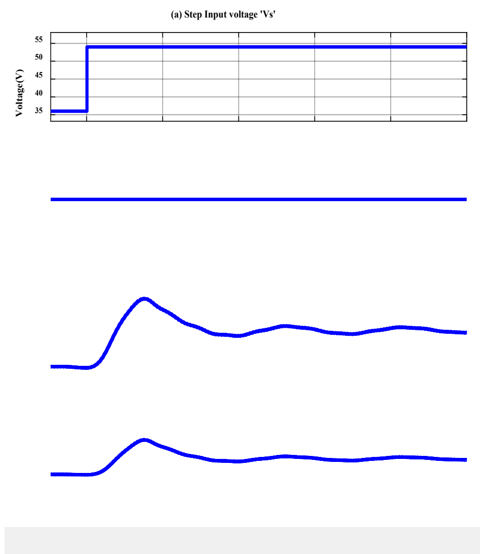

Figure 16. Dynamic performance of the NI-SC-SI-HG converter for a step input rise from 36V to 54V

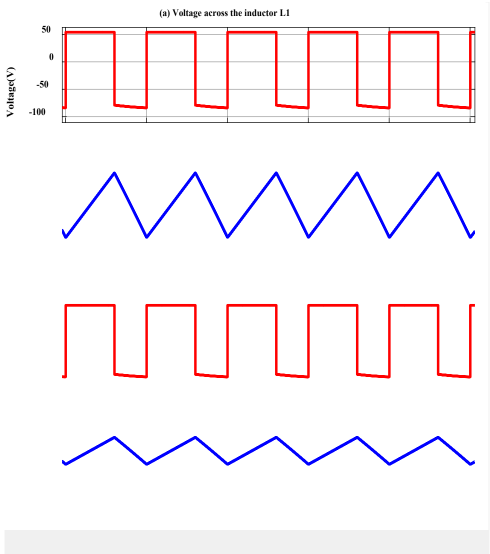

Figure 17. The voltage and current waveforms of L_1 and L_2

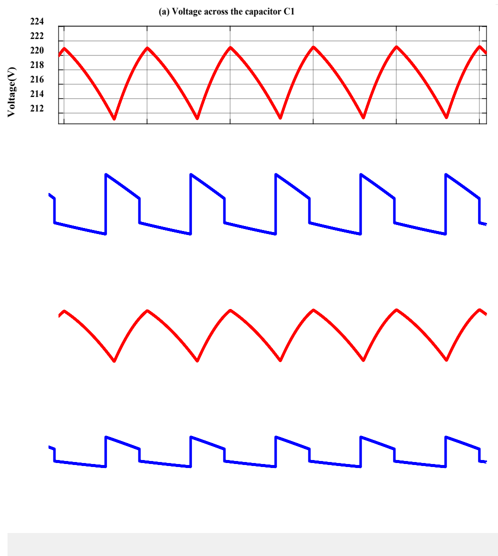

Figure 18. The voltage and current waveforms of C_1 and C_2

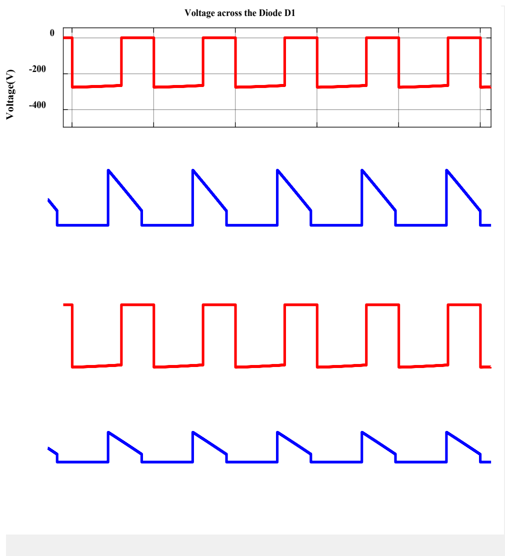

Figure 19. The voltage and current waveforms of the D_1 and D_2

The inductor waveforms of the converter are shown in Figure 17. An input voltage of 54 V is directly applied to inductors L1 and L2. Due to the zero-resistance path, both inductors are charged linearly from 1.596 A to 4.528 A when switches T1 and T2 are in the ON state. When T1 and T2 are in the OFF state, the current changes more rapidly, resulting in a higher voltage across L1 and L2, and both inductors discharge linearly from 4.528 A to 1.603 A. The capacitor waveforms of the converter are also shown in Figure 17.

When T1 and T2 are ON, both capacitors discharge approximately linearly from 220.8 V to 211.4 V, with the current decreasing from -0.566 A to -1.77 A. Therefore, the selected capacitors must withstand voltages up to 300 V. During the OFF state of T1 and T2, the capacitors charge approximately linearly from 211.4 V to 220.8 V, with current through the capacitors following the same profile. The voltage and current waveforms of the diodes are shown in Figure 19. During the ON state of T1 and T2, both diodes are reverse-biased, and the diode currents are zero. In the NI-SC-SI-HG converter, the maximum reverse voltage across the diodes is -280 V for an input voltage of 54 V. When T1 and T2 are OFF, the maximum current through the diodes reaches 2.4 A for a load power of 220 W. During this OFF state, the maximum voltage across the switches is 130 V for the same input voltage. The NI-SC-SI-HG converter is capable of producing a very high voltage gain, maintaining an output of 380 V from a lower input voltage of 58 V.

This feature makes the converter well-suited for integrating low-voltage PV modules into a DC grid. The PV system with the high-gain converter is shown in Figure 20. The solar PV array consists of three modules, each rated at 18 V, giving a total voltage of 54 V, which serves as the input to the converter. The converter employs the NI-SC-SI-HG network to achieve the high voltage gain necessary to feed a 380 V DC microgrid.

A perturb-and-observe (P&O) MPPT control unit is integrated to extract maximum power from the PV source by regulating the switching of T1 and T2. The output is filtered using Lf and Co to deliver a stable DC voltage to the microgrid. To test the converter's performance under lower input voltage, it was connected to the low-voltage PV system, whose characteristics are shown in Figure 21.

The NI-SC-SI-HG converter was evaluated under varying irradiance conditions using the P&O MPPT algorithm. During the interval from 0.01 s to 0.02 s, an irradiance of 1000 W/m² was applied. Between 0.02 s and 0.03 s, the irradiance dropped to 500 W/m².

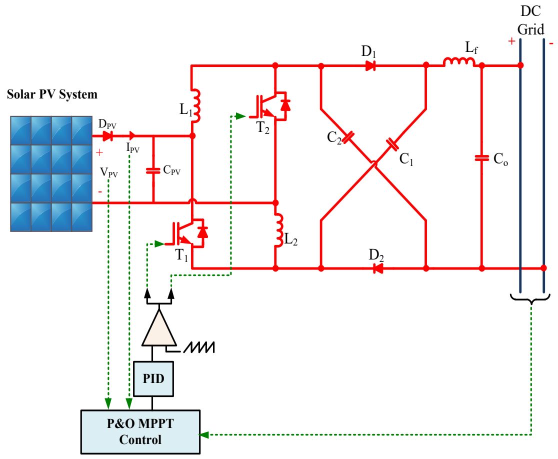

Figure 20. Circuit diagram of Solar PV System with NI-SC-SI-HG converter.

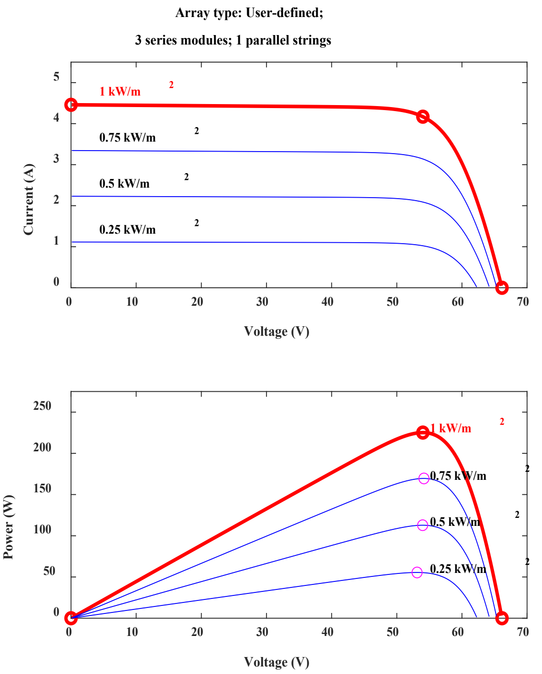

Figure 21. IV and PV characteristics of the PV system.

Subsequently, from 0.03 s to 0.04 s, the irradiance increased to 750 W/m². As shown in Figure 22, the power exported to the grid through the proposed converter was 225.18 W, 112.815 W, and 169.548 W at 1000, 500, and 750 W/m², respectively. The PV system responded rapidly to changes in irradiance, with only minor transient fluctuations in voltage and power during transitions. These oscillations reflect the MPPT algorithm's adaptation to new operating conditions. The level of solar irradiance directly influences both voltage and power output, highlighting its critical role in PV system performance. The system efficiently stabilizes after each irradiance change, ensuring consistent operation and reliable power export to the DC grid. Figure 22 effectively illustrates the PV system behavior under varying environmental conditions, demonstrating its ability to adjust to changes in irradiance while maintaining efficient voltage regulation and power delivery. Figure 22(a) shows the variation of solar irradiance over time. Initially, the irradiance is high, then drops sharply before rising to an intermediate level, reflecting changing sunlight intensity and its impact on system output. Figure 22(b) depicts the PV panel's voltage output over time. Despite fluctuations caused by changes in irradiance, the voltage remains relatively stable. Figure 22(c) shows the power delivered to the DC grid. As irradiance decreases, the power output drops correspondingly but stabilizes quickly, with transient fluctuations likely due to the MPPT algorithm adapting to changing solar input.

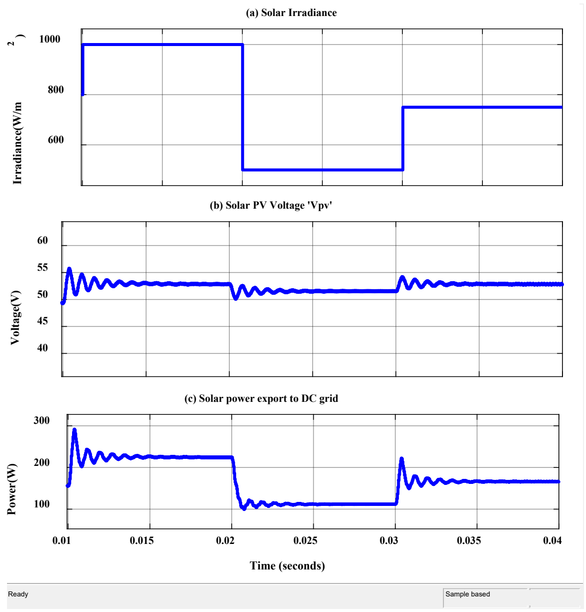

Figure 22. Voltage and current waveforms of the PV system

4.2. Experimental results

To analyze the performance of the NI-SC-SI-HG converter, a hardware setup was developed, and the results are presented in this section. The hardware setup of the NI-SC-SI-HG converter is shown in Figure 23. Initially, the inductor and capacitor values of the proposed converter were calculated using Equations (19) and (20), respectively. The ratings of the passive components depend on the duty ratio, input voltage (Vs), and load resistance (RL) connected to the converter. The switching frequency was chosen to be 50 kHz. For fast switching operation, the MOSFET IRFP260N was selected due to its suitability for high-speed switching and its ability to operate with a small power drive circuit. The hardware setup parameters are summarized in Table 2. A Micro-28377D microcontroller was used to generate high-frequency gating signals. This dual-core microcontroller from Texas Instruments' C2000 Delfino series can produce 3.3 V gate signals and is designed for high-performance real-time control applications. It is commonly used in power electronics, motor control, industrial automation, and automotive systems, and is based on the C28x DSP architecture.

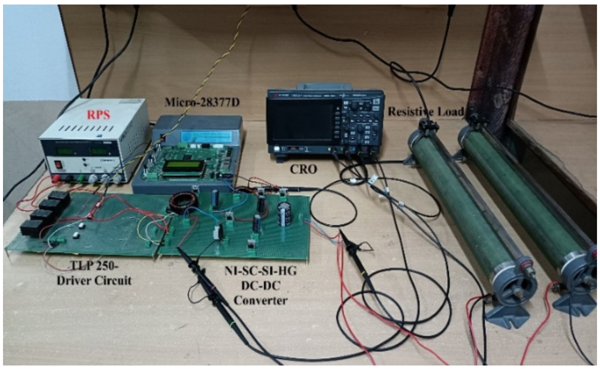

Figure 23. Hardware setup of the NI-SC-SI-HG converter

A TLP250 driver board was employed to protect the DSP controller from the power converter circuit. The driver board, in conjunction with the DSP controller, provides sufficient gate pulses to operate the power switches T1 and T2. The input voltage of 54 V is directly applied to the inductors. Due to the zero-resistance path, both inductors charge linearly when T1 and T2 are in the ON state. When the switches are turned OFF, the inductors discharge linearly, as shown in Figure 24(a). In the NI-SC-SI-HG converter, when both switches are ON, the voltage across the inductors remains constant, as illustrated in Figure 24(b), since the inductors are directly connected to the voltage source. When the proposed converter is excited by the input voltage, the output voltage is boosted to approximately seven times the input voltage at a duty ratio of 0.6, as shown in Figure 25(a). Simultaneously, both inductors are charged and discharged. The current waveform of L1 and the voltage waveform of C1 are illustrated in Figure 25(b). The NI-SC-SI-HG converter demonstrates high voltage gain, as evidenced by the significant scaling between the output and input voltages. Figure 26 presents experimental data confirming the voltage across the inductor while operating at the same duty ratio. Figure 25 summarizes the experimental results, showing the operating characteristics of various voltage ports, including the input, output, capacitor, and inductor voltages. A strong correlation is observed between the theoretical waveforms presented in this work and the experimentally recorded outcomes. The results demonstrate that the NI-SC-SI-HG converter can achieve high voltage gain even at low duty ratios.

Table 2. Proposed converter circuit parameters.

S. No.	Parameter	Value
1	Rated power (P_o)	220 W
3	Capacitors C_1 and C_2	1μF
4	Filter inductor L_f	2.2mH
5	Output capacitor C_o	1μF
6	Inductance L_1 and L_2	220μH
7	Capacitance C_1 and C_2	1μF
8	Switching Frequency 'f_{SW}'	50 kHz
9	MOSFET Switch	IRFP260 N
10	Microcontroller	Micro-28377D

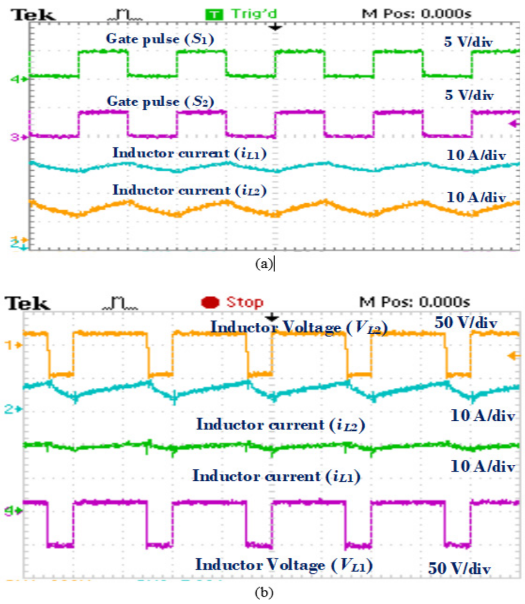

Figure 24. Hardware results for fixed duty ratio.(a) current through inductors (b) voltage across the inductors

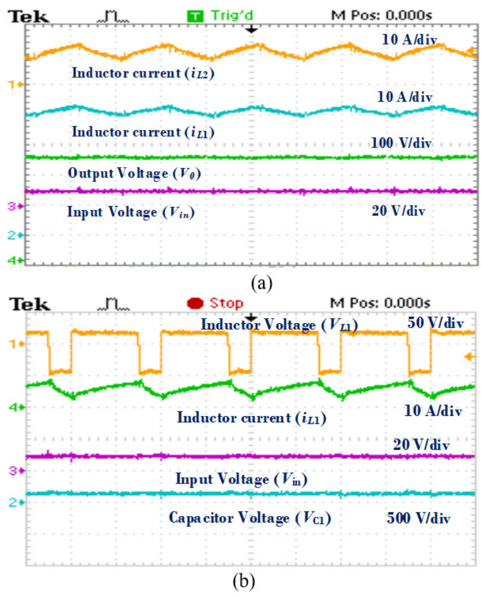

Figure 25. Experimental results (a) current waveform of inductors.

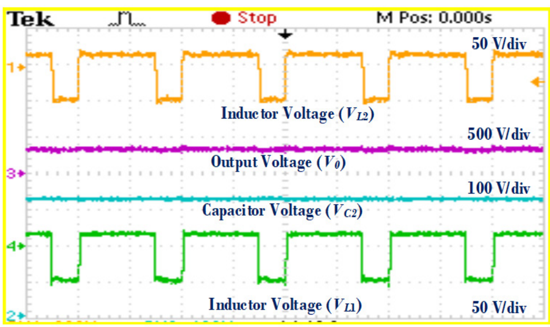

Figure 26. Experimental results - voltage across the inductors, capacitor, and load.

5. CONCLUSIONS

The NI-SC-SI-HG converter can achieve a voltage gain of 7 at a duty ratio of 0.6, which is approximately three times higher than that of a conventional boost converter. It can generate an output voltage of 380 V from a low input voltage, making it well suited for microgrid applications. Additionally, the converter is ideal for low-voltage renewable energy systems, such as solar PV applications. When tested under varying irradiance conditions, the NI-SC-SI-HG converter maintained a stable DC output of 380 V while efficiently exporting power to the grid. Based on detailed operational analysis, mathematical derivations, and hardware results from a 220 W laboratory prototype, the converter achieved an average conversion efficiency of over 93% and a maximum efficiency of 96.6%.

Across a wide range of operating conditions, including different duty cycles, the NI-SC-SI-HG converter outperforms previously reported boost topologies in terms of voltage gain and switch voltage stress. Future research will focus on further enhancing system efficiency by integrating the NI-SC-SI-HG converter with advanced control strategies.

6. ACKNOWLEDGEMENT

The authors are incredibly grateful to the authorities of the involved educational institutions for financially supporting this research.

NOMENCLATURE

LV	Low Voltage
PV	Photo Voltaic
DC	Direct Current
MPPT	Maximum Power Point Technique
CCM	Continues Conduction Mode
DCM	Discontinues Conduction Mode
SC	Switched Capacitor
SI	Switched Inductor
HG	High Gain
HV	High Voltage
ESR	Equivalent Series Resistance
LV	Low Voltage

REFERENCES

1. Abedi, A., Rezaie, B., Khosravi, A., & Shahabi, M. (2020). A Novel Local Control Technique for Converter-Based Renewable Energy Resources in the Stand-Alone DC Micro-Grids. Journal of Renewable Energy and Environment, 7(2), 52-63. https://doi.org/10.30501/jree.2020.107365

2. Ansari, M. S., Rath, I. C., Patro, S. K., Shukla, A., & Bahirat, H. J. (Jan.-Feb 2023). High power parallel hybrid DC-DC converter. IEEE Transactions on Industry Applications, 59(1), 1077–1089. https://doi.org/10.1109/tia.2022.3217026

3. Asapu, S., Juttiga, L., Bhuvaneswari, D., Adabala, S. S., Apireddi, P., & Bale, A. (2024). Implementation of Seven-Level Asymmetrical Multilevel Inverter for Solar PV Application. International Conference on Distributed Computing and Optimization Techniques (ICDCOT), 1–5. https://doi.org/10.1109/icdcot61034.2024.10516167

4. Asapu, S., Palleswari, Y. T. R., Rapaka, P. S., Bade, M. C., Deenakonda, M., & Banothu, R. (2024). Design and Implementation of High Voltage Gain DC-DC Converter for solar PV Applications. International Conference on Computational Intelligence for Green and Sustainable Technologies (ICCIGST), 1–5. https://doi.org/10.1109/iccigst60741.2024.10717566

5. Axelrod, B., Berkovich, Y., & Ioinovici, A. (2008). Switched-capacitor/switched-inductor structures for getting transformerless hybrid DC–DC PWM converters. IEEE Transactions on Circuits and Systems. I, Regular Papers: A Publication of the IEEE Circuits and Systems Society, 55(2), 687–696. https://doi.org/10.1109/tcsi.2008.916403

6. Bagheri, S. , & Moradi CheshmehBeigi, H. (2022). DC Microgrid Voltage Stability Through Inertia Enhancement Using a Bidirectional DC-DC Converter. Journal of Renewable Energy and Environment, 9(3), 32-44. https://doi.org/10.30501/jree.2021.298032.1233

7. Banaei, M. R., & Ajdar Faeghi Bonab, H. (2018). A transformerless high step-up conversion ratio dc–dc converter with voltage multiplier. EPE Journal, 29(1), 38–48. https://doi.org/10.1080/09398368.2018.1548803

8. Bheemraj, T. S., Anil Kumar, Y., Karthikeyan, V., & Pragaspathy, S. (2023). A hybrid structured high step-up DC–DC converter for integration of energy storage systems in military applications. IEEE Transactions on Circuits and Systems. II, Express Briefs: A Publication of the IEEE Circuits and Systems Society, 70(4), 1545–1549. https://doi.org/10.1109/tcsii.2022.3225900

9. Do, H.-L. (2011). Integrated ZVS DC–DC converter with continuous input current and high voltage gain. International Journal of Electronics, 98(9), 1199–1214. https://doi.org/10.1080/00207217.2011.593135

10. Fallahzadeh, S. A. A. , Abjadi, N. Reza, Kargar, A. , & Blaabjerg, F. (2021). Applying Sliding-Mode Control to a Double-Stage Single-Phase Grid-Connected PV System. Journal of Renewable Energy and Environment, 8(1), 1-1. https://doi.org/10.30501/jree.2020.233358.1114

11. Gholizadeh, H., & Ben-Brahim, L. (2022). A New Non-Isolated High-Gain Single-Switch DC–DC Converter Topology with a Continuous Input Current. Electronics, 11(18), 2900. https://doi.org/10.3390/electronics11182900

12. Guo, R., Liang, Z., & Huang, A. Q. (2011). A high efficiency transformerless step-up DC-DC converter with high voltage gain for LED backlighting applications. 2011 Twenty-Sixth Annual IEEE Applied Power Electronics Conference and Exposition (APEC), 1350–1356. https://doi.org/10.1109/apec.2011.5744767

13. Wu, G., Ruan, X., & Ye, Z. (2018). High step-up DC–DC converter based on switched capacitor and coupled inductor. IEEE Transactions on Industrial Electronics (1982), 65(7), 5572–5579. https://doi.org/10.1109/tie.2017.2774773

14. Hasanpour, S., Siwakoti, Y. P., & Blaabjerg, F. (2023). A New High Efficiency High Step-Up DC/DC Converter for Renewable Energy Applications. IEEE Transactions on Industrial Electronics, 70(2), 1489–1500. https://doi.org/10.1109/TIE.2022.3161798

15. Lakshmi, M., & Hemamalini, S. (2018). Nonisolated High Gain DC–DC Converter for DC Microgrids. IEEE Transactions on Industrial Electronics, 65(2), 1205–1212. https://doi.org/10.1109/tie.2017.2733463

16. Lung-Sheng Yang, Tsorng-Juu Liang, & Jiann-Fuh Chen. (2009). Transformerless DC–DC Converters With High Step-Up Voltage Gain. IEEE Transactions on Industrial Electronics, 56(8), 3144–3152. https://doi.org/10.1109/tie.2009.2022512

17. Mahmood, A., Zaid, M., Ahmad, J., Khan, M. A., Khan, S., Sifat, Z., Lin, C.-H., Sarwar, A., Tariq, M., & Alamri, B. (2021). A Non-Inverting High Gain DC-DC Converter With Continuous Input Current. IEEE Access, 9, 54710–54721. https://doi.org/10.1109/access.2021.3070554

18. Mansour, A. S., Amer, A.-H. H., El-Kholy, E. E., & Zaky, M. S. (2022). High gain DC/DC converter with continuous input current for renewable energy applications. Scientific Reports, 12(1). https://doi.org/10.1038/s41598-022-16246-8

19. Natarajan Vijayanathan, S., Ahmad Khan, I., Anbazhagan, L., Vishnuram, P., & Bajaj, M. (2024). Multi-Input DC-DC Converter for Nanogrid Integration with Solar Photovoltaic Systems. Journal of Renewable Energy and Environment, 11(4), 157-164. https://doi.org/10.30501/jree.2024.447204.1867

20. Nie, S., Zhang, J., Xiao, W., & Du, G. (2025). High-gain DC-DC converter with ultra-low input voltage*. Chinese Journal of Electrical Engineering, 11(1), 74–82. https://doi.org/10.23919/cjee.2025.000096

21. Rajesh, R., Prabaharan, N., & Santhosh, T. K. (2023). Design and Analysis of a Non-Isolated DC-DC Converter With a High-Voltage Conversion Ratio. IEEE Transactions on Circuits and Systems II: Express Briefs, 70(6), 2036–2041. https://doi.org/10.1109/tcsii.2022.3226187

22. Siva, A., Palleswari, Y. T. R., Kadali, K. S., Bhukya, R., Deenakonda, M., & Inti, V. V. V. (2024). Single-Phase Grid and Solar PV Integration with 15-Level Asymmetrical Multilevel Inverter. Cognitive Computing and Cyber Physical Systems, 37–47. https://doi.org/10.1007/978-3-031-48891-7_3

23. Salimi, M., & Pornadem, M. (2018). A modular transformerless DC-DC step-up converter with very high voltage gain and adjustable switch stress. EPE Journal, 28(2), 75–88. https://doi.org/10.1080/09398368.2018.1425526

24. Salvador, M. A., Lazzarin, T. B., & Coelho, R. F. (2018). High Step-Up DC–DC Converter With Active Switched-Inductor and Passive Switched-Capacitor Networks. IEEE Transactions on Industrial Electronics, 65(7), 5644–5654. https://doi.org/10.1109/tie.2017.2782239

25. Tang, Y., Wang, T., & Fu, D. (2015). Multicell switched-inductor/switched-capacitor combined active-network converters. IEEE Transactions on Power Electronics, 30(4), 2063–2072. https://doi.org/10.1109/tpel.2014.2325052

26. Yari, K., & Hasanpour, S. (2024). A Minimum Phase DC-DC Converter with Continuous Input Current and High Voltage Gain. https://doi.org/10.22541/au.171359264.42760641/v1

27. Heidari Beni, S., Mirtalaei, S. M. M., Kianpour, A., & Aghababaei Beni, S. (2017). Design and improvement of a soft switching high step-up boost converter with voltage multiplier. IET Power Electronics, 10(15), 2163–2169. https://doi.org/10.1049/iet-pel.2017.0162